Frequency Domain EMI-Simulation and Resonance Analysis of a DCDC-Converter

P. Hillenbrand*, M. Böttcher, S. Tenbohlen
Institute of Power Transmission and High Voltage Technology (IEH), University of Stuttgart
Stuttgart, Germany
*philipp.hillenbrand@ieh.uni-stuttgart.de

J. Hansen*
Automotive Electronics
Robert Bosch GmbH
Schwieberdingen, Germany
*jan.hansen@de.bosch.com

***Abstract*—This paper proposes a frequency domain model to predict conducted electromagnetic interferences (EMI) caused by a converter. In the model, the nonlinear and time-variant semiconductor switches of the converter are replaced by voltage sources characterized by measurements during operation of the converter. A vector network analyzer (VNA) measurement method is presented to characterize the disturbance path from the voltage sources to the line impedance stabilization network (LISN). The approach shows that the main resonances of the disturbance voltage at the LISN are caused by the coupling path, which is linear and time-invariant. Based on this knowledge, a frequency domain simulation of the coupling path is performed. The simulation reproduces the measured coupling path very well. Based on the analysis of the electromagnetic potential at selected resonance frequencies, an electrical circuit is designed that accurately describes EMC root-causes of the converter.**

Keywords— conducted emissions, behavioral voltage sources, multi-port network model, equivalent network

I. INTRODUCTION

Electromagnetic compatibility (EMC) in the field of full and hybrid electrical vehicles is a rising topic [1]. Prediction of conducted and radiated emissions of traction inverters is important for car and component manufacturer especially in an early development stage of the product. Therefore, there are plenty of simulation models to estimate both kinds of emissions. These models can be grouped in two parts: transient simulations [2] and frequency domain simulations [3-8]. With the ability to model time-variant and non-linear elements, transient simulations cover potential EMC issues more accurately than frequency domain simulations. However, simulation time steps need to be very short at high frequencies and sharp rise and fall times, and the total simulation time needs to be quite long to reach a steady state of the system. The simulation time thereby rises with the dimensions of the test setup. Concerning the dimensions of the CISPR 25 test setup simulation models in frequency domain are absolutely necessary to predict emissions above 30 MHz in practical time durations [1].

There are several frequency domain simulation models for inverter EMI in the literature, which approximate non-linear source characteristics by linear modelings. On the one hand, there are physics-based equivalent circuit models, e.g. [5]. These models are often used to simulate either common-mode (CM) [6] or differential-mode (DM) [7] noise, i.e. they are valid if one of both can be identified as dominating. Under these circumstances, the switches are replaced by a single CM or DM noise source. The main advantage of these models is their simplicity, which allows a profound understanding of all relating phenomena. On the other hand, there are modular-terminal-behavioral (MTB) models like [3], [4]. These "black-box" models can produce very accurate simulation results with little information about the internal structure of the modeled device. However, they are less suitable to get a good understanding of the source and propagation of the emissions and cannot be used to optimize a device towards lower EMI.

This contribution presents a "white-box" model to combine the advantages of physics-based equivalent circuit models and MTB models. Therefore, the nonlinear semiconductor switches of a given converter are replaced by behavioral voltages sources, Fig.1. Similar to a MTB model, the voltage sources are characterized during operation of the converter.

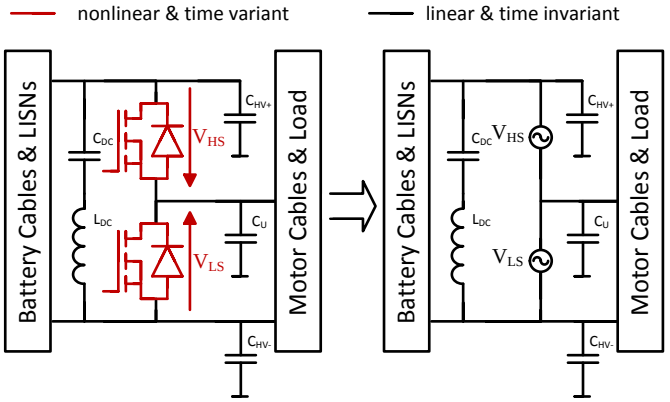

Fig. 1. Replacement of nonlinear and timevariant lowside and highside switches by two ideal voltage sources in frequency domain.

The coupling path from each of the two voltage sources towards the LISN is measured with a VNA and combined with the measured voltage sources. This method is used to analyze whether the replacement of the switches by the measured sources is valid or not. Afterwards, a 3D geometry model is presented to simulate the coupling path. Based on the simulation model, a physics-based equivalent circuit is derived by analyzing the electromagnetic potential at selected resonance frequencies. The resulting circuit provides accurate simulation results of the conducted emissions and can be used for root-cause analysis of the converter EMI.

II. Test Setup

A. Description of the Silicon Carbide MOSFETs Inverter

This contribution uses the test setup presented in [6] to investigate the conducted emissions of an automotive inverter. Similar to the case defined in CISPR 25, the setup consists of two LISNs, the inverter, and a three-phase load (3~load) which are mounted on a conductive table and connected to each other using unshielded cables. In contrast to [6], the investigated inverter uses silicon carbide (SiC) MOSFETs. Fig. 2 pictures the main PCB of the Inverter (a) and the cooling of the semiconductors (b). For simplicity reasons, the inverter is reduced to one half-bridge, yielding a DCDC-converter configuration. One leg of the 3~load is connected to the half-bridge, the remaining two legs are linked to HV-. The 3~load consists of three inductances which are connected to a star and three discrete capacitances towards the housing of the load. To limit the load current of the DCDC-converter, one resistor is added in series with each of the three inductances.

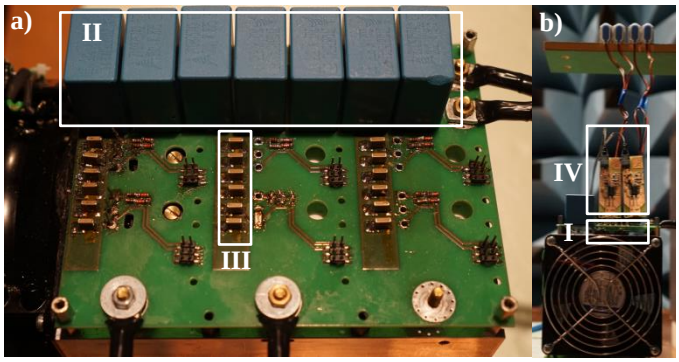

Fig. 2. a) main PCB b) front perspective of the cooling of the inverter

The half-bridge consists of two SCT2080KE SiC-MOSFETs (I) produced by Rohm™ with a maximum drain current of 40 A and a breakdown voltage of 1.2 kV. Both switches are connected to a DC-link capacitor of 17.2 µF. The capacitor is built up with seven 2.2 µF electrolyte capacitors (II) and 18 100 nF ceramic capacitors (III) which are placed very close to the switches. To minimize the influence of the control electronics, battery supplied gate-units (IV) with optical fiber- transmitted control signals are used at the top of the main PCB.

B. Disturbance Voltage at the LISN during operation of the converter

The DC-voltage V_{DC} applied to the DC link capacitor is set to 192 V for all following measurements and simulations. The half-bridge operates at a pulse width frequency of f_{PWM} = 10.1 kHz, a duty cycle of 7 % and a blanking time of t_b = 1.6 µs, which avoids a short circuit of the DC-link capacitor during switchover.

During the operation of the inverter, the disturbance voltages, V_{HV+} and V_{HV-}, at the LISNs are measured using an oscilloscope in time-domain. Afterwards, the measured data is transformed into frequency-domain using an FFT-algorithm. Fig. 3 shows the measurement results. The high frequencies are measured with a 20 MHz high-pass filter to achieve a sufficient signal-to-noise ratio.

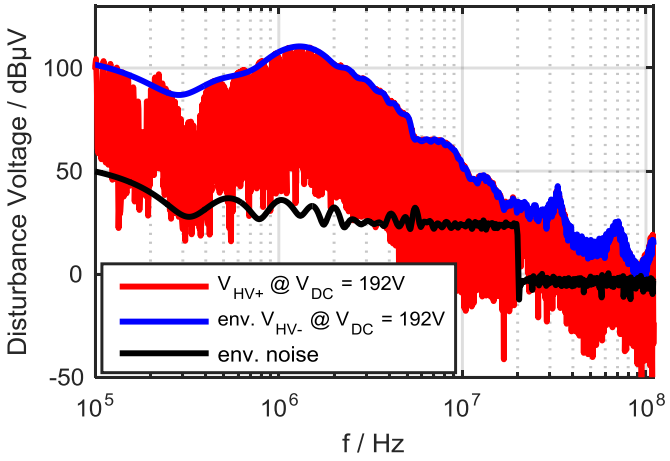

Fig. 3. FFT of disturbance voltages V_{HV+} and V_{HV-} at the LISN, measured in time-domain during operation of the DCDC-converter. [env. = envelope]

III. Determination Of The Noise Sources

To characterize the behavioral voltage sources V_{HS} and V_{LS} shown in Fig. 1, the voltages across the high-side and low-side switches of the converter are measured during operation. For the model, both magnitude and phase of the voltage sources are relevant. Because of that, both voltages are measured simultaneously in time domain. In equal manner to the measurement of the disturbance voltage at the LISNs, the signals are measured with an oscilloscope and transformed afterwards into frequency-domain. To minimize the influence of the voltage probe, it is necessary to use a high-impedance probe. It is advantageous if the probe shows a high pass characteristic. Fig. 4 shows the measured magnitude of the high-side and low-side voltage for the operating point described in Section II B. For better differentiation, V_{LS} is displayed as the peak envelope of 50 adjacent data points.

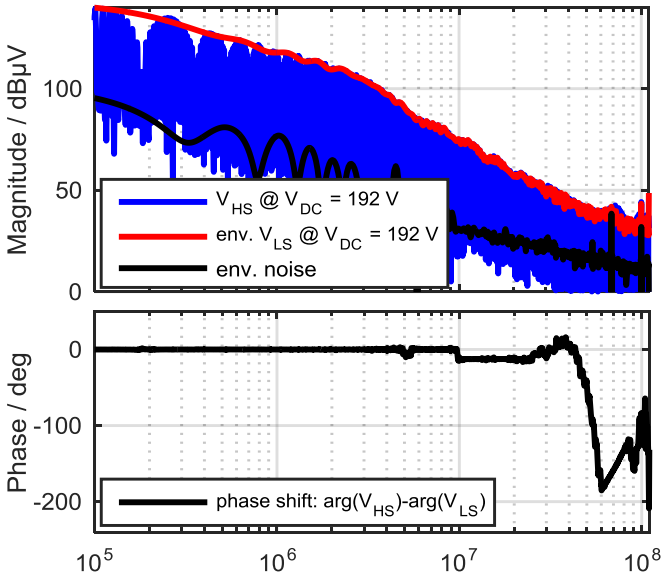

Fig. 4. Voltage frequency spectrum of high-side and low-side switches during operation of the DCDC-converter (V_{DC} = 192 V, f_{PWM} = 10.1 kHz, 7% duty cycle) [env. = envelope]

The measurement results of the magnitudes, Fig. 4, show that both voltages are very similar to the spectrum of a trapezoidal pulse. Below 40 MHz the phase difference between both voltages is close to zero. In this frequency range the noise sources can be described as a common-mode source concerning the orientation of the voltages pictured in Fig. 1. Above 40 MHz the phase shift varies between 0 and 180 deg. In this frequency range both common and differential mode excitation are present.

IV. Characterizing The Disturbance Path

In a real test setup, it is hardly possible to estimate all essential parasitic elements to create a detailed equivalent circuit of the test setup. Therefore, a VNA measurement method is presented to characterize the frequency behavior of the linear time-invariant (LTI) system components without knowing any specific element. Based on the principle depicted in Fig. 1, both switches are regarded as ideal voltage sources. According to the superposition principle, the effect of one ideal voltage source can be calculated individually with all other voltage sources short-circuited. Consequently, the LTI system between the voltage sources and the LISN can be represented by voltage transfer functions. One transfer function for each voltage source V_{HS} and V_{LS} is measured for one LISN port with the principle shown in Fig. 5. During excitation at one switch, the other switch is short-circuited through the gate unit.

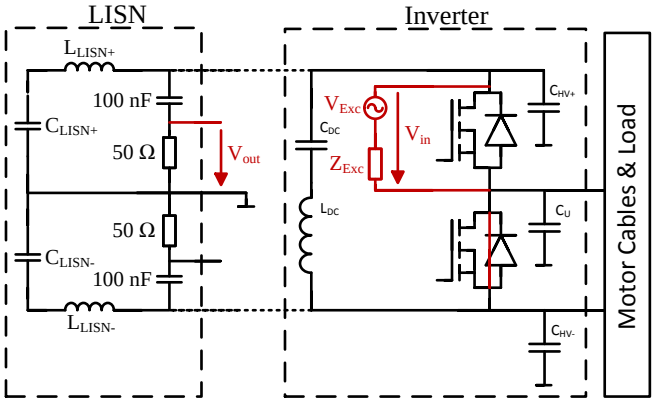

Fig. 5. Measurement setup of the voltage transfer function form the high-side switch to the LISN with short circuited low-side switch.

We obtain the transfer function as the ratio of the measured and the input voltage,

$$TF_{\mathrm{HS}\rightarrow\mathrm{LISN+}} = \frac{V_{\mathrm{out}}}{V_{\mathrm{in}}} \tag{1}$$

In the literature different measurement methods are described to measure a voltage transfer function with the help of a VNA. For the existing test setup we considered that the differential excitation at the switch has to be galvanically isolated from the single-ended measurement at the LISN. The traditional approach for this problem is to convert the balanced port to a single-ended port using a balun. The two major disadvantages of this technique are non-ideal isolation and limited bandwidth of the balun, particularly when characterization over a wide frequency range is necessary [10]. Another possibility is to run the VNA galvanically isolated from the measurement table with one port directly connected to the switch and the other port connected to the LISN with an analog fiber optic link. Here, the critical aspects are the bandwidth of the fiber optic link and the isolation of the VNA supply. More accurate measurements can be achieved with three single ended VNA ports in the setup pictured in Fig. 6. Port 1 and port 2 are connected to drain and source of the high-side switch, respectively, and port 3 is connected to the LISN.

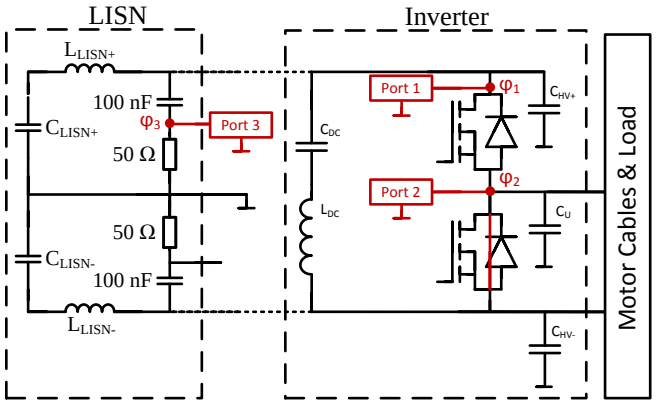

Fig. 6. VNA measurement setup with three single ended ports.

In this test setup, the transfer function can be calculated from the scattering parameter data [S]. One possible way is the mixed-mode calculation presented in [10], where two single-ended ports are transformed to one differential port. In this scenario the port impedance of the differential port has to be considered, which is equal to the sum of two single-ended ports. With the correct port impedance, the voltage transfer function can be calculated from the reflection at the differential port between port 1 and 2 and the response at port 3. A simpler way is the direct calculation of the transfer function using the admittance matrix [Y] calculated by equation (2) with the unit matrix [E].

$$[\mathrm{Y}] = \frac{1}{Z_0}([\mathrm{E}] + [\mathrm{S}])^{-1} \cdot ([\mathrm{E}] - [\mathrm{S}]) \tag{2}$$

The transfer function is independent of the impedance between port 1 and port 2. Consequently, a virtual ideal current source of 1 A is used as excitation at the switch. According to Kirchhoff's current law, the potentials at the ports can then be described with (3), and calculated with (4), as follows:

$$[\mathrm{Y}] \cdot \vec{\varphi} = \vec{\mathrm{I}} \rightarrow \vec{\varphi} = [\mathrm{Y}]^{-1} \cdot \vec{\mathrm{I}}, \tag{3}$$

$$\begin{pmatrix} \varphi_1 \\ \varphi_2 \\ \varphi_3 \end{pmatrix} = \begin{bmatrix} \begin{pmatrix} Y_{11} & \cdots & Y_{13} \\ \vdots & \ddots & \vdots \\ Y_{31} & \cdots & Y_{33} \end{pmatrix} \end{bmatrix}^{-1} \cdot \begin{pmatrix} 1 \\ -1 \\ 0 \end{pmatrix} \tag{4}$$

The voltage transfer function defined in (1) can then be calculated with the resulting potentials and equation (5):

$$TF_{\mathrm{HS}\rightarrow\mathrm{LISN+}} = \frac{\varphi_3}{\varphi_2 - \varphi_1}. \tag{5}$$

Measurement setup and calculation can be checked by applying a DC-voltage to the converter. A voltage of less than 10 V mostly changes the voltage dependent capacitance of the switch and the scattering parameter data significantly. However, with a correct calculation and measurement setup, the voltage transfer function should remain identical. Fig. 7 shows the measurement result of the transfer functions of the low-side and high-side voltage source towards LISN+.

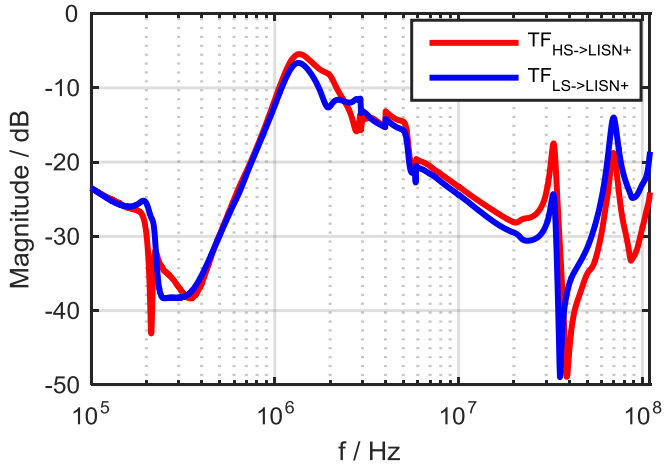

Fig. 7. Measurement result of the transfer functions measured with a VNA

With the information of the voltage sources and the disturbance path towards the LISN, it is possible to calculate the disturbance voltage spectrum at the LISN by (6). Fig. 8 shows the calculation result compared to the measured disturbance voltage during the operation of the converter.

$$V_{HV+,calc} = TF_{HS\rightarrow LISN+} \cdot V_{HS} + TF_{LS\rightarrow LISN+} \cdot V_{LS} \quad (6)$$

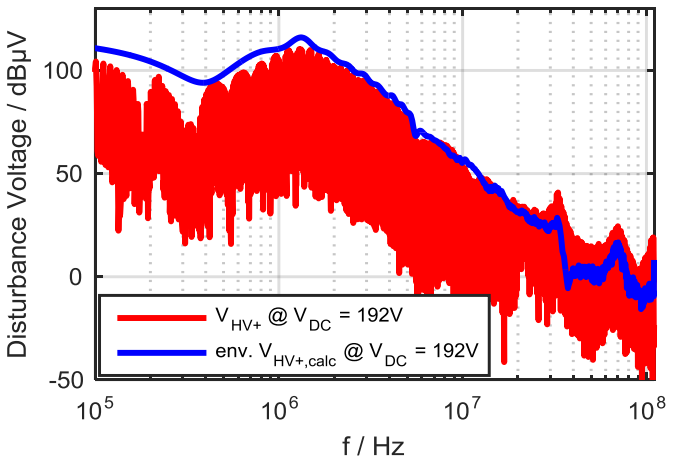

Fig. 8. Comparison of measured and calculated disturbance voltage [env. = envelope].

The calculation of the disturbance voltage reproduces the measurement very well in the complete frequency range from 0.15 to 110 MHz. This proves the validity of replacing the semiconductor switches by measured voltage sources. The magnitudes of the disturbance voltage at the LISN show a similar shape compared to the measured transfer functions. This allows the conclusion that the main resonances of the disturbance voltage at the LISN are caused by the linear and time-invariant disturbance path. This is investigated further in the following simulation.

V. Simulation Of Coupling Path

A coupling path simulation is performed using a two-step computer simulation. First, a geometry model is created, which exhibits the key geometric features of the measurement setup. This model comprises the measurement table, LISNs, load box, wiring, a PCB model, and models of the packages of the switches as well as the styrofoam (blue), on which the setup is placed, Fig. 9. Excitation ports are set at the end points of all wires, at the positions of all capacitors, and between source and drain of each switch. The model is discretized by a tetrahedral mesh. Based on model order reduction, a broadband frequency-domain electromagnetic field computation is performed, resulting in a multi-port network model which characterizes the electromagnetic properties of the geometry model. Secondly, this model is applied in a circuit simulator, where S-Parameter data of the DC-link capacitors, of 3~load and LISNs are attached to the multiport model. As in the measurements, one of the switches is short-circuited (represented by the $R_{DS,on}$ of the closed switch), and the other is equipped with a broadband voltage source in frequency domain. The simulations are carried out in the CST Studio Suite [9] on an HP Z820 Workstation with 128 GB RAM. The electromagnetic simulation takes about 12 minutes in the frequency range from 0.3 to 110 MHz. However, the subsequent circuit simulation needs several seconds only.

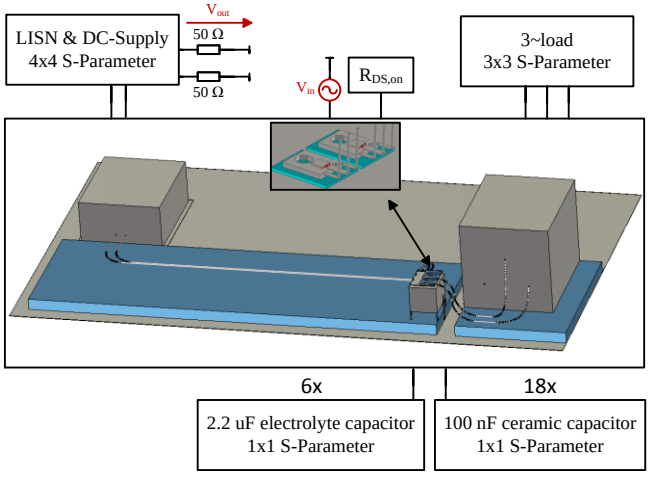

Fig. 9. 3D-geometry of the simulation model.

The computed transfer function by the above described model is shown in Fig. 10, in comparison with the measured one. The mismatch is a smaller than 5 dB from 0.3 to 110 MHz. In the model, a short circuited switch is represented by its on-resistance ($R_{DS,on}$). This value has a strong influence to the magnitude of the TF below 1 MHz. For this model, the value is measured outside the test setup with a different gate-unit which causes the small deviations at lower frequencies.

Taking advantage of the electromagnetic simulation, we now use the computer model to study the resonances A and B in the spectrum displayed in Fig. 10. In particular, we use the

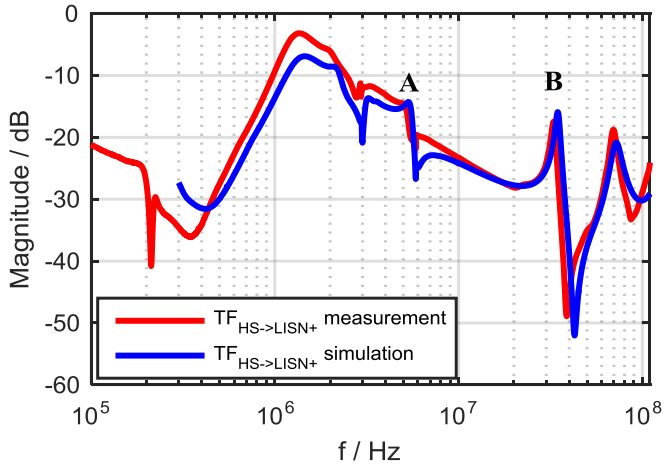

Fig. 10. Comparison of measured and simulated transfer functions.

method proposed in [11] to discover the root-cause of these resonances. The resonances are explained with the aid of a physically reduced equivalent electrical circuit (PHREEC), i.e., an electrical circuit in which the capacitances and inductances correspond to those parts of the model geometry, which are the root-causes of the resonances. The derivation of the PHREEC's topology is hereby essential. In an electrical circuit, the circuit nodes are locations of constant potential; by contrast, on a location $\vec{x}$ within a 3D-structure, the electromagnetic potential $\varphi(\vec{x})$ is, along with the vector potential $\vec{A}(\vec{x})$, a continuous quantity [14]. However, at resonance frequencies, we can often localize maxima and minima of the electromagnetic potential clearly. In this case, the approximation of the 3D- structure by a PHREEC is admissible, and we set a single circuit node each in maximum and minimum [11]. Finally, the value of the capacitances that causes the resonance can be estimated by an electrostatic solver [9] or by the method explained in [12]. The partial inductances that span the corresponding loops are computed using the algorithm described in [13].

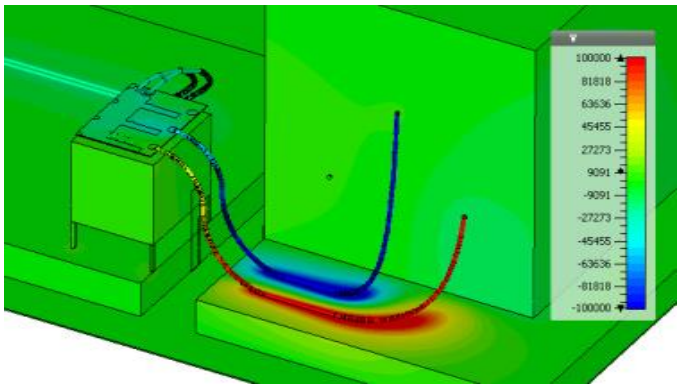

Fig. 11. Electromagnetic potential of resonance A: the wires with their load box capacitances resonate with each other. Loadbox, cooler, and table are of almost constant potential.

The electromagnetic potential at the resonances A and B is shown in Fig. 11 and Fig. 12 and is computed by the CST Studio Suite. At resonance A (shown in Fig. 11) we recognize the wires to carry maximum and minimum potential. In fact, at the wire ends in the loadbox there are 2 nF capacitors located; the inductances corresponding to the resonances are the wires and the PCB, with PCB plus and minus short-circuited due to the excitation (one switch is short circuited, the other switch is attached to a voltage source with no series impedance). At resonance B (shown in Fig. 12), the positive maximum of the potential is the PCB itself, whereas the negative one is the entire ground structure, i.e., table, loadbox, and cooler.

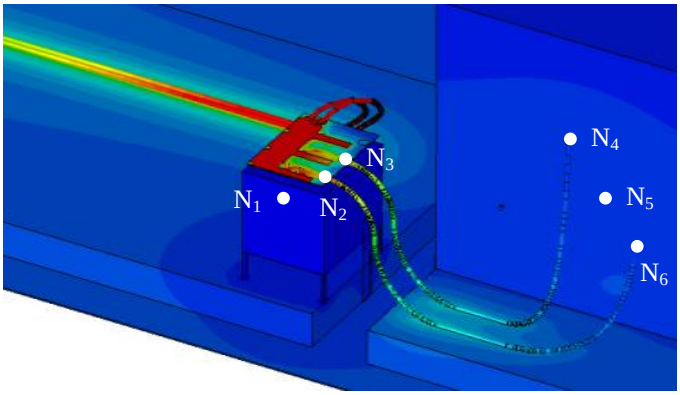

Fig. 12. Electromagnetic potential of resonance B: The PCB with attached wires resonates with the entire ground structure of loadbox, table, and cooler. Both are approximately surfaces of equal potential, shortened at LISN side.

Based on this insight we derive a PHREEC topology and circuit as in Fig. 13: We set circuit nodes at each end of the wires (N_1, N_3, N_4, N_6), as well as one on the loadbox in between the wire ends (N_5) and one on top of the cooler (N_1), Fig. 12. Computing the partial inductance matrix of this system, we obtain two partial inductances for the wires and one inductance for the ground return path. The partial inductances are calculated as L_{Cable_U} (N_2-N_6), L_{Cable_W} (N_3-N_4) and L_{Ground} (N_1-N_5) including the inductive coupling to each other. Finally, the capacitance values $C_{Load,U}$ and $C_{Load,W}$ are known by loadbox construction, and the capacitances C_{HV+}, C_U, and C_{HV-} are computed by a static solver. The computed capacitances include the capacitances of the switches, the PCB and the connected cable.

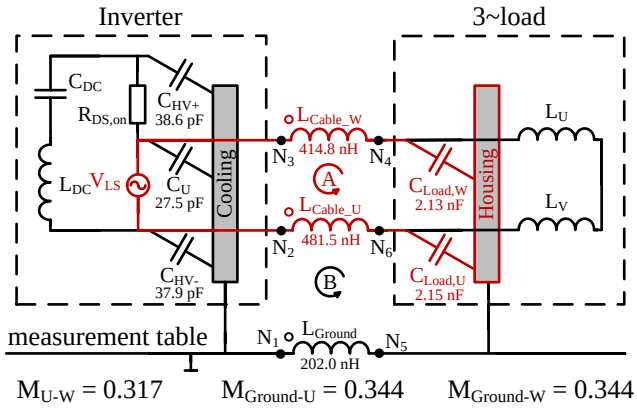

Fig. 13. Equivalent circuit derived from potential analysis of modes A and B.

Fig. 13 shows the resulting equivalent circuit which combines the involved elements of resonance A and B. The circuit is further extended by the elements of the LISN as well

as the battery cables and implemented in a Spice simulation. Fig. 14 compares the transfer function from the high-side switch to the LISN based on the circuit simulation and the 3D geometry.

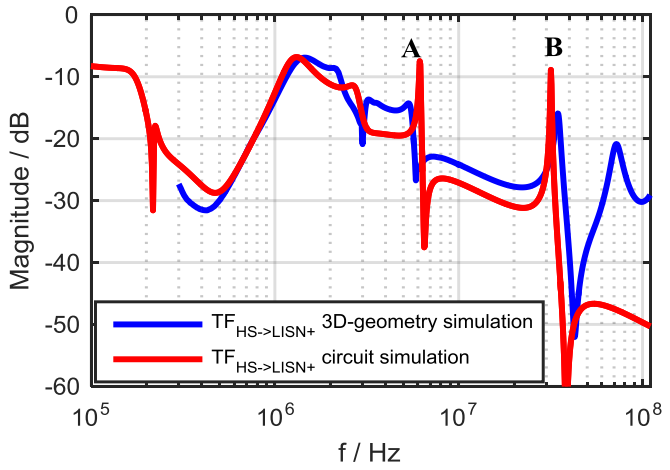

Fig. 14. Comparison of simulated transfer function with 3D-geometry model compared to the simulation of the derived equivalent circuit

Looking at resonance A and B, the results show a similar shape of the voltage transfer function. The slight deviations of the resonance frequencies are caused by the inaccurate position of the nodes N_1 to N_6 and the higher Q factor of the resonances in the circuit simulation are caused by the approximation of the load capacitances without series resistance and series inductance. Above 50 MHz, the circuit does not match the 3D-simulation since the next resonance at about 70 MHz is not considered in the PHREEC topology design.

Based on the circuit presented in Fig. 13, the resonances A and B can be explained in detail. Resonance A is caused by a series resonance of $L_{\text{Cable\_U}}$, $L_{\text{Cable\_W}}$, $C_{\text{load,U}}$ and $C_{\text{load,W}}$ with a resonance frequency of 6.2 MHz. At the resonance frequency, there is a local maximum of the differential mode current between both motor cables. This current result in a large voltage drop between N_2 and N_5 due to the higher inductance of $L_{\text{Cable\_U}}$ compared to $L_{\text{Cable\_W}}$. This phenomenon is also known as DM-to-CM conversion. The LISN and the battery cables are connected in parallel to these two points and show therefore a high voltage drop at that frequency. Secondly, resonance B is caused by a CM-resonance of both motor cables connected in parallel, the inductance of the ground path, and the capacitances inside the inverter. This resonance between the inverter and the 3~load is well described in [6], but is shifted towards higher frequencies because of the much smaller parasitic capacitances inside the inverter investigated in this work.

It is also interesting to note that below 600 kHz, the circuit model shows identical behavior as the 3D-model, as both differ here from the measurement. Precisely, apart from a rough estimation of LISN wire inductances, the circuit and the 3D-model do not share any common information in this low frequency range. Here, reflection at the high-side switch is very close to 1 caused by very low inductance of the DC-link capacitor and the short circuited low side-switch. Hence, the measurement and the simulation are very sensitive with respect to small resistances, which can differ in measurement and simulation models.

VI. Conclusion

This paper proposes a new frequency-domain model for conducted EMI of a converter. The model is designed by replacing the nonlinear and time-variant semiconductor switches of the converter by behavioral voltage sources, characterized by measurements during operation of the device. To verify the approach, voltage transfer functions from the sources to the LISN are measured with a VNA in the real test setup. Combining the transfer functions with the voltage sources allows the reproduction of the disturbance voltage at the LISN and justifies the method. Subsequently, the transfer functions are simulated based on a 3D-model. A geometry model of the complete CISPR 25 test setup is combined with S-Parameter data of the LISNs, load and discrete parts of the inverter. The simulation reproduces the measured coupling path very well. Based on the resonances of the electromagnetic potential, a physical equivalent circuit is developed which accurately describes the root-causes of the EMI resonances.

References

[1] J. Schanen, J. Roudet (2008): "Built-in EMC for integrated power electronics systems," in Integrated Power Systems (CIPS), 2008 5th International Conference on , pp.1-10.

[2] S. Niedzwiedz, S. Frei (2013): "Transient emission analysis of EV- and HEV-powertrains using simulation" in International Symposium on Electromagnetic Compatibility (EMC EUROPE) 2013 pp.247-252.

[3] Q. Liu, F. Wang, D. Boroyevich (2006): "Modular-Terminal-Behavioral (MTB) Model for Characterizing Switching Module Conducted EMI Generation in Converter Systems" in: IEEE Transanctions On Power Electronics, Vol. 21, No. 6, p. 1804-1814.

[4] M. Foissac, J. Schanen, C. Vollaire (2009): "Black box EMC model for power electronics converter" in Energy Conversion Congress and Exposition, pp.3609-3615.

[5] Meng Jin; Ma Weiming; Zhang Lei (2004): "Determination of noise source and impedance for conducted EMI prediction of power converters by lumped circuit models," in Power Electronics Specialists Conference IEEE 35th Annual, vol.4, pp.3028-3033.

[6] P. Hillenbrand, C. Keller, S. Spanos, S. Tenbohlen (2015): "Understanding Conducted Emissions from an Automotive Inverter Using a Common-Mode Model" in IEEE and EMC Europe Joint Conference, Dresden.

[7] L. Ferrer, J. Balcells, D. Gonzalez, J. Gago, M. Lamich (2003): "Modelling of differential mode conducted EMI generated by switched power inverters" in Industrial Electronics Society vol.3, pp.2312-2315.

[8] A. Domurat-Linde, E. Hoene (2010): "Investigation and PEEC based simulation of radiated emissions produced by power electronic converters" in Integrated Power Electronics Systems (CIPS), 2010 6th International Conference, pp.1-6.

[9] CST Studio Suite, www.cst.com.

[10] Agilent Technologies (2002): "An Introduction to Multiport and Balanced Device Measurements" in Multiport and Balanced Device Measurement Application Note Series, Application Note 1373-1.

[11] F. Traub, J. Hansen, W. Ackermann, Th. Weiland (2013): "Eigenmodes of electrical components and their relation to equivalent electrical circuits", IEEE Symp. on EMC, pp. 287 – 293.

[12] J. Hansen, C. Potratz (2015): "Capacity Extraction in Physical Equivalent Networks", IEEE Symp. on EMC, pp. 491 – 496.

[13] F. Traub, J. Hansen, W. Ackermann, Th. Weiland (2013): "Automated construction of physical equivalent circuits for inductive components", EMC Europe, pp. 67-72.

[14] C. Balanis (2012): "Advanced engineering electromagnetics", 2nd edition, Hoboken, pp. 256-257.